Electronic Supplementary Material (ESI) for Sustainable Energy & Fuels.

A Hybrid Molecular Photoanode for Efficient Light Induced Water Oxidation

Sergi Grau,[a,#] Serena Berardi,[a,#,*] Alicia Moya,[c] Roc Matheu,[a] Vito Cristino,[b] Juan José Vilatela,[c] Carlo A. Bignozzi,[b] Stefano Caramori,[b] Carolina Gimbert-Suriñach,[a,*]Antoni Llobet[a,*]

(a) Institute of Chemical Research of Catalonia (ICIQ), Barcelona Institute of Science and Technology (BIST), Avda. Països Catalans 16, 43007, Tarragona, Spain

(b) Dept. of Chemistry and Pharmaceutical Sciences, University of Ferrara, Via di Mortara 17, 44121, Ferrara, Italy.

(c) IMDEA Materials Institute, c/. Eric Kandel 2, 28906, Getafe, Madrid, Spain

[#]These authors contributed equally to this work

*Corresponding authors

Supporting Information

Table of Contents

Materials and methods

1- Materials and Methods

General

Buffer solutions were prepared with Na_2HPO4, NaH_2PO_4 from Sigma-Aldrich. Metallic W (99.95%, Alfa Aesar), hydrogen peroxide (30%, Honeywell Fluka) and Triton X-100 (Fluka) were used as received. The molecular ruthenium precursor of Ru-WOC was prepared following a described procedure in the literature.[1] ITO substrates were purchased from Delta Tech (Corning® alkaline earth boroaluminosilicate glass, 50 x 75 x 1.1 mm, indium tin oxide coated on surface, Rs = 4 - 10 Ω/sq), FTO substrates were purchased from Pilkington (FTO TEC 8, 8 Ω/sq).

Atomic force microscopy (AFM) images were collected using a Digital Instruments Nanoscope III scanning probe Microscope (Digital Instruments, CA). The instrument was equipped with a silicon tip (RTESP-300 Bruker) and operated in tapping mode. Surface topographical analysis of raw AFM images was carried out with NanoScope analysis 1.5 program.

Scanning Electron Microscopy (SEM) images were obtained using a Zeiss Evo 40 electron microscope.

X-ray Diffractometry (XRD) analysis was carried out with an automatic Philips X'pert $\theta/2\theta$ diffractometer using Cu KR radiation (λ = 1.5416 Å).

UV-Vis measurements were carried out on a Lambda 1050 PerkinElmer spectrophotometer equipped with a PMT, InGaAs and PbS detectors system, double beam optics, double monochromator and D2 and W light sources. Diffuse reflectance measurements were carried out in the same equip using 150mm Integrating Sphere with PbS and PMT detectors.

Electrochemical equipment

Cyclic voltammetry (CV), linear sweep voltammetry (LSV) and bulk electrolysis (BE)) were measured using a CHI660D potentiostat or CHI730D bipotentiostat.

The oxygen evolution experiments based on the Generator-Collector method were done using a CHI730D bipotentiostat.

Electrochemical Impedance Spectroscopy (EIS) analyses were performed using a PGSTAT-302N potentiostat, equipped with a FRA2.v10 frequency response analyzer and controlled by Nova 1.10. An Abet solar simulator, equipped with an AM1.5G filter and calibrated to 0.1 W/cm^2 using a Newport 1918-C Power Meter, was used as the illumination source. The illuminated photoanodes were sampled in the selected potential ranges (0.14-0.94 V vs NHE) at 50 or 100 mV intervals. A 10 mV amplitude sinusoidal perturbation, whose angular frequency ω ranged between 50000 and 0.05 Hz, was used (single-sine frequency scan mode for ω > 2.6 kHz and 5-sine frequency scan mode for ω < 2.6 kHz). The EIS data were fitted by means of the equivalent circuit reported in Figure S13 using the ZView software with typical relative errors lower than 10%.

Preparation of WO_3/$BiVO_4$ photoanodes

0.46 g of metallic W were added to 5 mL of 30% H_2O_2 and stirred until the dissolution was completed. 2 drops of Triton-X were then added, and the resulting solution was spin coated (at 1000 rpm for 9 s, then at 2000 rpm for 20 s) on the top of cleaned FTO slides. Three spin coating cycles were performed, each one followed by an annealing step at 550°C for 15 min. The AFM characterization of the resulting electrodes confirms the compact nature of the so-deposited WO_3 film (Figure S1). Mesoporous WO_3 was then formed on the top of the WO_3 compact underlayer, by spin-coating a colloidal precursor (prepared following literature procedures)[2] at 600 rpm for 6 s, then at 2000 rpm for 20 s. Six spin coating cycles were performed, each one followed by an annealing step at 550°C for 30 min. Finally, $BiVO_4$ was electrodeposited on the top of the so-produced electrodes, following an adapted literature procedure.[3] Figures S2-S5 summarize the optical, electrochemical, structural and morphological characterization of the full $WO_{3(C)}/WO_{3(P)}/BiVO_4$ photoelectrode.

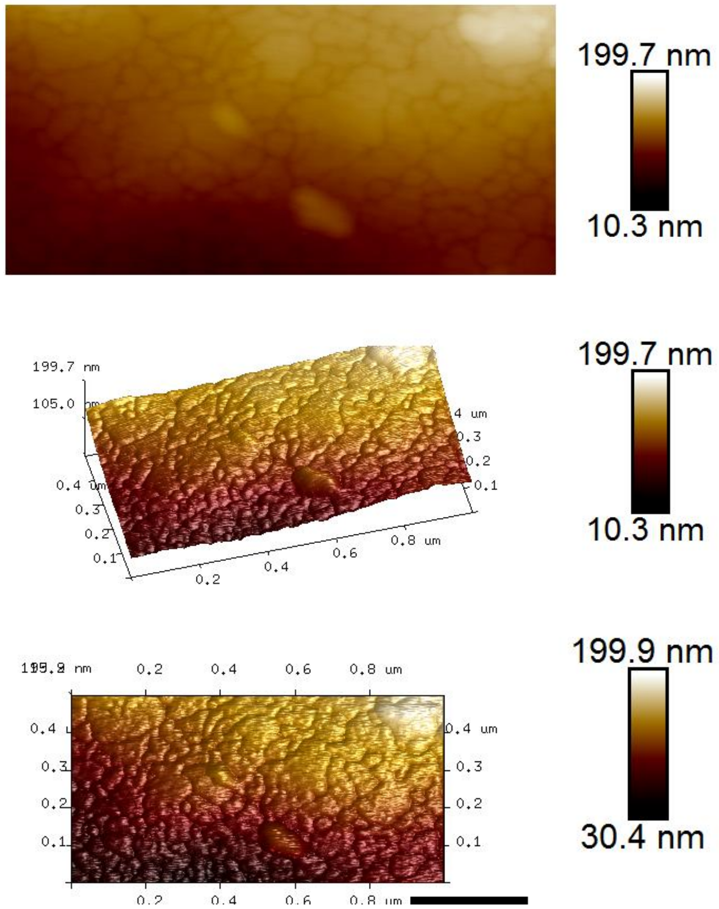

Figure S1. AFM images of the WO_3 compact underlayer deposited on FTO.

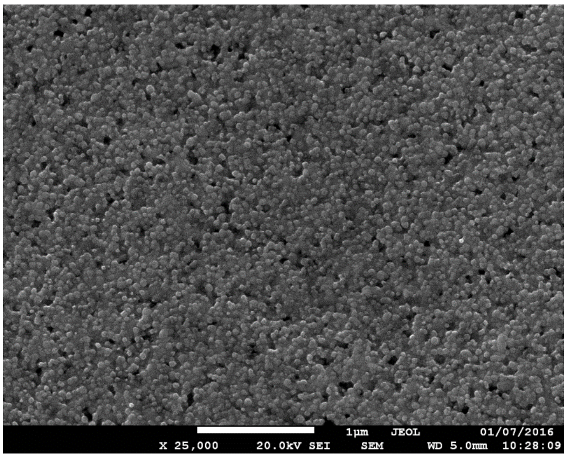

Figure S2. SEM image of a $WO_{3(C)}/WO_{3(P)}/BiVO_4$ photoelectrode evidencing the WO_3 particles (with diameters of 50-70 nm) homogeneously covered by $BiVO_4$

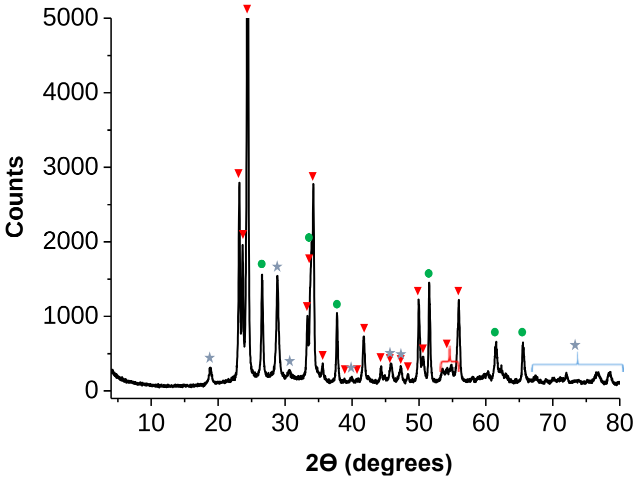

Figure S3. Grazing incidence XRD difractogram of $WO_{3(C)}/WO_{3(P)}/BiVO_4$ photoelectrode. Red triangles: WO_3; grey stars: $BiVO_4$; green circles: FTO.

In order to determine the optical band gap of $WO_3/BiVO_4$ the diffuse reflectance UV-vis spectra were measured. Kubelka-Munk equation (eq 1) can be used to extract the absorption coefficient (α) from the diffuse reflectance spectra:[4]

$$f(R) = \frac{(1-R)^2}{2R} = \frac{\alpha}{s} \qquad \text{(eq 1)}$$

Where R is diffuse reflectance values at given wavelength and *s* is the scattering coefficient.

Assuming that *s* is wavelength independent, we can consider that *f(R)* is directly proportional to α, and *f(R)* can be used in place of α to make the Tauc plot (eq 2):

$$\alpha h\nu \propto (h\nu - E_g)^{\frac{1}{n}} \qquad \text{(eq 2)}$$

Where E_g is band gap energy (in eV) and *n* can take value of ½ for the direct and allowed transition.

Plotting $(\alpha h\nu)^2$ vs $h\nu$ (Tauc plot) E_g value can be calculated extrapolating the linear region to the baseline (Fig S4). The value obtained using this method gives an E_g value of 2.6 eV that is in good agreement with the reported values for $BiVO_4$ thin films (2.5-2.6 eV).[5]

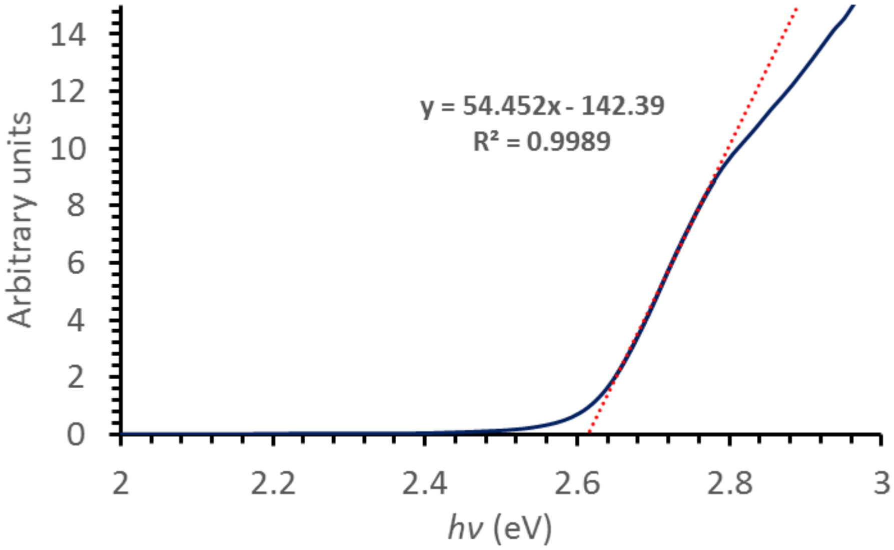

Figure S4. Tauc plot and corresponding fitting.

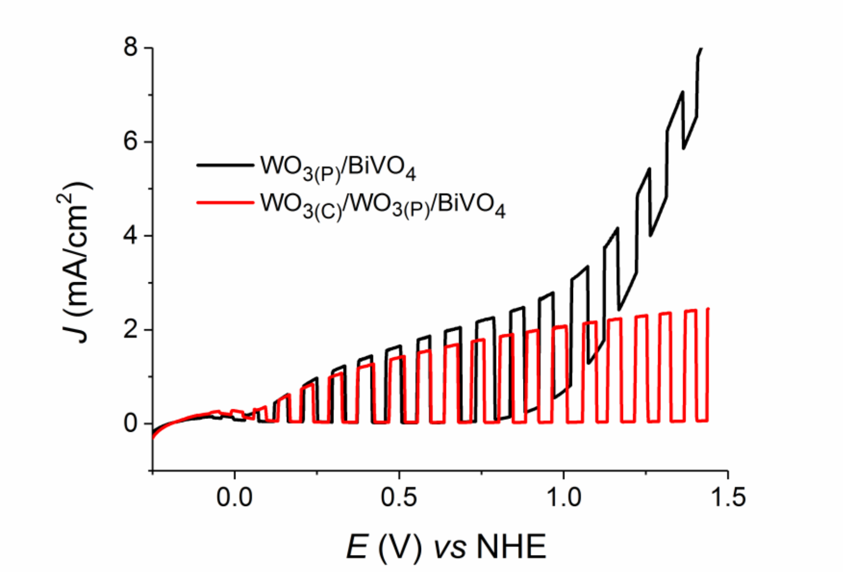

Figure S5. Chopped light LSV of a $WO_{3(C)}/WO_{3(P)}/BiVO_4$ (red) and $WO_{3(P)}/BiVO_4$ (black) electrodes in the presence of a sacrificial agent (0.1 M Na_2SO_3 at pH 7), scan rate = 10 mV/s. $WO_{3(C)}$ = compact tungsten oxide film, $WO_{3(P)}$ = mesoporous tungsten oxide layer. The onset of the transient photocurrent (at *ca.* -0.05 V vs NHE) gives an estimation of the conduction band position. The dark current of the full electrode $WO_{3(C)}/WO_{3(P)}/BiVO_4$ (red) is negligible in all the explored potential range as opposed to the electrode that lacks the WO_3 compact underlayer $WO_{3(P)}/BiVO_4$ (black).

Fabrication of carbon nanotube fibers (CNT_f)

The CNT fiber layer consisted of a thin planar array of multiple CNT fibers overlaid as a non-woven unidirectional fabric. The CNT fibres were produced by directly spinning of a CNT aerogel from the gas-phase during CNT growth by chemical vapour deposition at 1250°C.[6] Butanol, ferrocene, thiophene and hydrogen were used as carbon source, catalyst promoter and carrier gas, respectively. Their concentration was fixed to produce CNTs of few layers (3-5) length of around a millimeter. In the fiber, the CNTs are strongly associated in bundles that thus enable swift stress and charge transfer. Yet, the bundles are imperfectly packed and lead to a large mesoporosity and high surface area.

Preparation of $WO_3/BiVO_4/CNT_f/Ru$-WOC photoanodes

First, the $WO_3/BiVO_4$ photoanodes were cleaned with deionized water and dried with airflow. CNT_f is an extremely thin black foil (Figure S6, pic 1), placed between two protective paper foils. The most convenient way to cut it is using scissors before removing the paper foils (Figure S6, pic 3). After removing the paper (Figure S6, pic 5), the piece of appropriate size is placed on the surface of the photoanode with Teflon tweezers. Finally, a drop of acetone is added, wetting the whole fiber (Figure S6, pic 7). It is advisable to hold the edges of the CNT_f when acetone is added to prevent the CNT_f getting folded or rolled up (Figure S6, pic 6). The position of the CNT_f can be readjusted while still being wet (Figure S6, pic 8). Rolling a glass pipette to pull out the excess of acetone helps to get a flat and well attached CNT_f layer (Figure S6, pic 9-11). With the addition of acetone the CNT_f is contracted and gets attached on the photoelectrode surface in a relatively stable way. It is important that the CNT_f doesn't touch the edge of the $BiVO_4$ photoanode (or uncovered FTO), otherwise CNT_f may be in contact with FTO, creating a short-circuit between the back contact (FTO) and the layer in contact with the electrolyte (CNT_f/Ru-WOC) (Figure S6, pic 11 and 12).

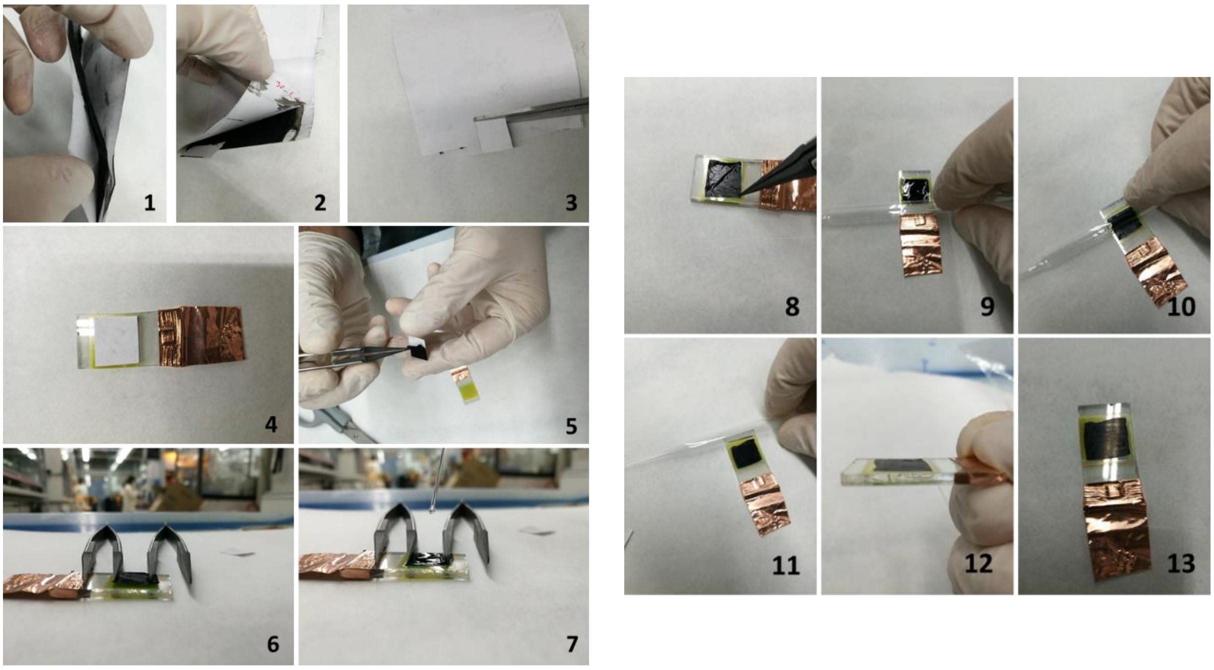

Figure S6. Deposition of CNT_f films on the $WO_3/BiVO_4$ photoanodes.

Photoelectrochemistry (PEC)

All the electrochemical and photoelectrochemical experiments were performed in a pH 7 phosphate buffer (Ionic strength = 0.5M) and using a hand-made Teflon cell (Figure S7). Platinum coil was used as counter electrode and $Hg/HgSO_4$ or SCE as reference electrodes (the potentials were converted to NHE by applying a correction of +0.645V or +0.240 respectively). The teflon cell allows to illuminate the sample either from the front or from back. In our system, we use only back illumination since the carbon nanotube fibers (CNTf) are black and opaque. The cell also allows to perfectly control the photoanode's area exposed to the electrolyte and to the light and corresponds to a 0.5 cm^2 area.

A Xenon Lamp (Abet LS150) with a UV-light filter (cutoff <400nm) was used as a source of light unless otherwise stated. The light intensity reaching the electrode was calibrated to 1 sun by means of a silicon photodiode, independently calibrated using a solar simulator (AM1.5G of solar radiation with a total light intensity of 100 mW/cm^2).

To perform the chopped light LSV, automated handmade chopper was used, changing between dark and light conditions every 5 seconds.

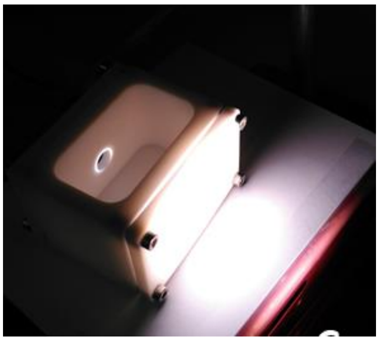

Figure S7. Photoelectrochemical cell used in this work.

Oxygen detection experiments using the Generator-Collector method [7,8]

The Generator-Collector method consists of placing two electrodes very near to each other. One of them will perform water oxidation (Generator) while the other is set to reduce the oxygen that is produced (Collector) (Figure 11, Left).

In our setup, the photoanode (*e.g.* $WO_{3(C)}/WO_{3(P)}/BiVO_4/CNT_f$/Ru-WOC) acts as an oxygen Generator. The Collector electrode consist of a clean FTO (sonicated for 15min in a saturated solution of KOH in 2-propanol, rinsed with water and annealed for 30 min at 500ºC). To select the optimal potential to reduce molecular oxygen in solution, several CVs in pH7 were performed in aired and degassed solutions (Fig S11, Right). A reduction peak controlled by diffusion can be observed in aired solution, reaching the maximum intensity at -0.355V vs NHE.

Both electrodes are placed together with the conductive part facing the inner part of the set-up. Two small pieces of coverslip (Menzel-Gläser, 130-140µm of thickness) are used to keep a constant distance between both electrodes. Then the electrodes are covered with parafilm leaving lateral apertures in both sides to allow the solution to fill the inner space by capillarity forces (Fig S11, Left). Finally, the reference electrode is placed as near as possible to one lateral aperture.

To determine at witch potential the $WO_{3(C)}/WO_{3(P)}/BiVO_4/CNT_f$/Ru-WOC and $WO_{3(C)}/WO_{3(P)}/BiVO_4$ (Generators) start to produce molecular oxygen, LSV at 5mV/s under 1 sun illumination were performed in a degassed pH7 solution while the Collector performs a controlled potential electrolysis at -0.355V vs NHE.

To determine the faradaic efficiency of the experiment using the Generator-Collector method is necessary to assess the Efficiency of Oxygen Reduction of the set-up by using a generator electrode that is known to generate 100 % Faradaic efficiency. In our work, we used a FTO electrode modified with cobalt oxide, prepared using an adapted reported methodology.[8,9] For details on the faradaic efficiency calculation, please go to pages S12-S13.

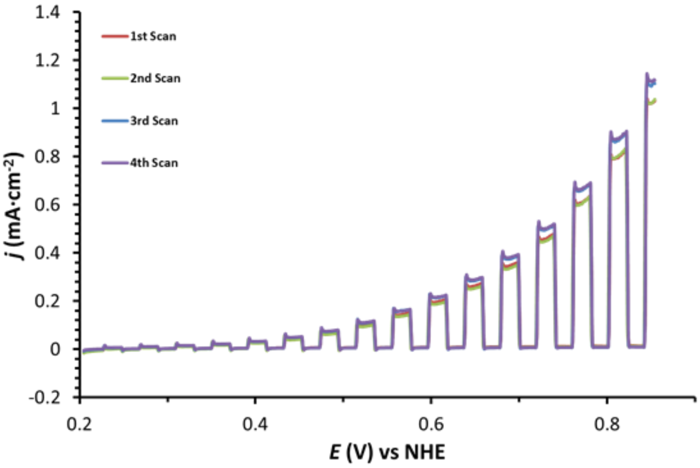

Figue S8. Consecutive LSV experiments (scan rate = 5 mV/s) of $WO_3/BiVO_4$ photoanodes showing an improving of its performance. All electrodes were submitted to such consecutives LSV until they were identical (usually takes 3-5 scans). After these LSV pre-treatment the photoanode is ready to be covered with CNT_f.

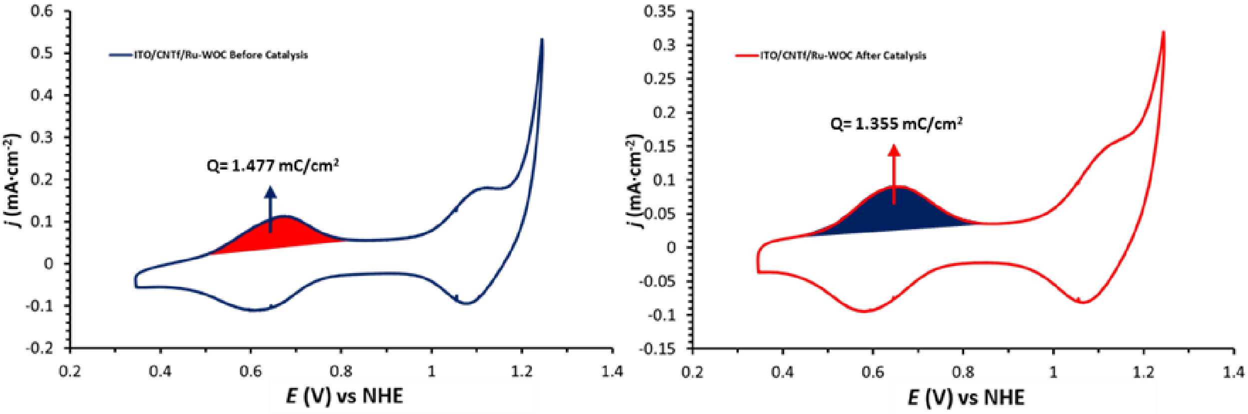

Figure S9. CV (5mV/s) of a ITO/CNT_f/Ru-WOC electrode. **Left)** as deposited. **Right)** After a 10 minutes bulk electrolysis at E_{app} = 0.645 V vs NHE at pH 7 of a $WO_3/BiVO_4/CNT_f$/Ru-WOC photoanode and subsequent transfer of the CNT_f/Ru-WOC film on a clean ITO substrate. The surface coverage (Γ) of the Ru-WOC precursor on the FTO/CNT_f electrodes was estimated by applying the formula Γ (mol·cm^{-2}) = Q /(n*S*F), where Q is the charge under the Ru(III/II) oxidation wave, n is the number of electrons involved in the electron transfer (1 e^- in this case), S is the surface of the electrode (0.5 cm^2) and F is the faradaic constant. Interestingly, after the bulk electrolysis experiment, only the ruthenium complex precursor is observed. The absence of the redox features of the Ru-aquo derivative (true Ru-WOC) is likely explained by the fast equilibrium between the two species that is favored at neutral pH and at low oxidation states.[1,10-12]

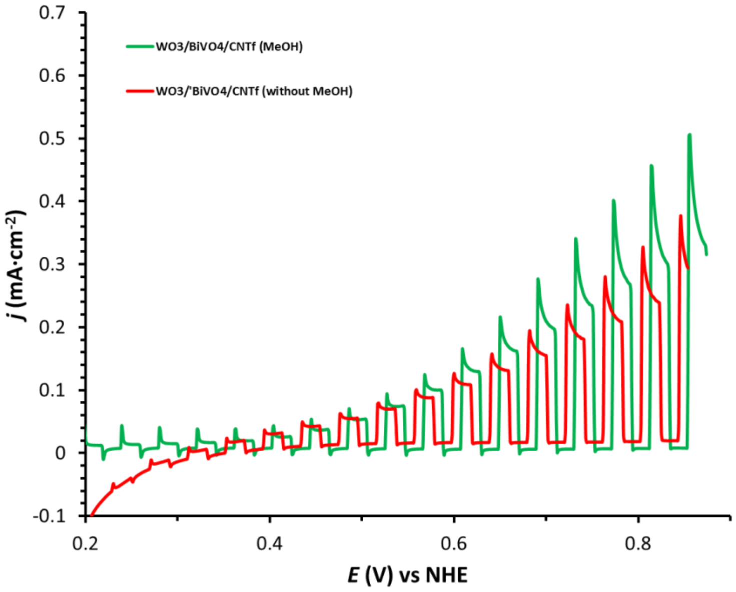

Figure S10. Comparison of the performance of a $WO_3/BiVO_4/CNT_f$ photoanode with (green) and without (red) treatment with methanol.

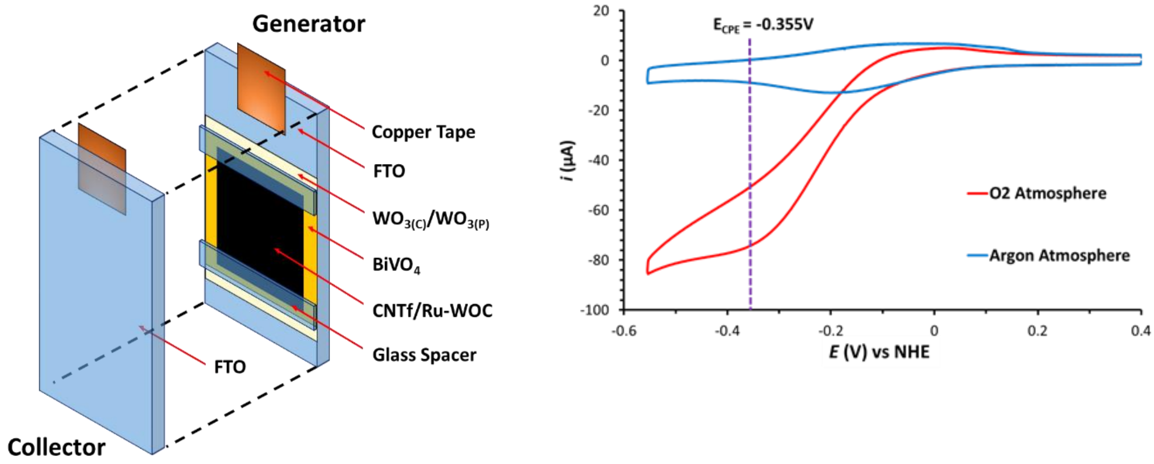

Figure S11. Left) Scheme of Generator-Collector system used in this work. **Right)** Cyclic voltammograms of an FTO working electrode in pH 7 under argon or oxygen atmosphere to set the potential for oxygen reduction in the collector electrode.

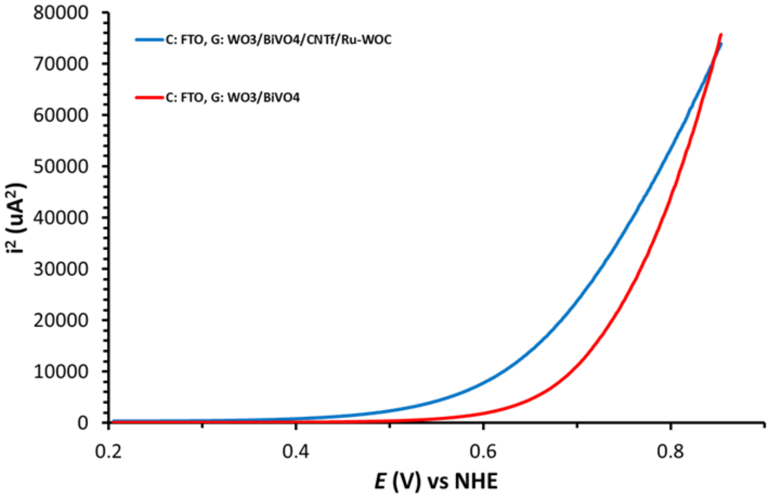

Figure S12. Plot of i^2 vs applied potential of a controlled potential electrolysis experiment using the Generator(G)-Collector(C) Method (from Figure 4 of main manuscript). This figure helps recognizing the onset point of the catalysis.

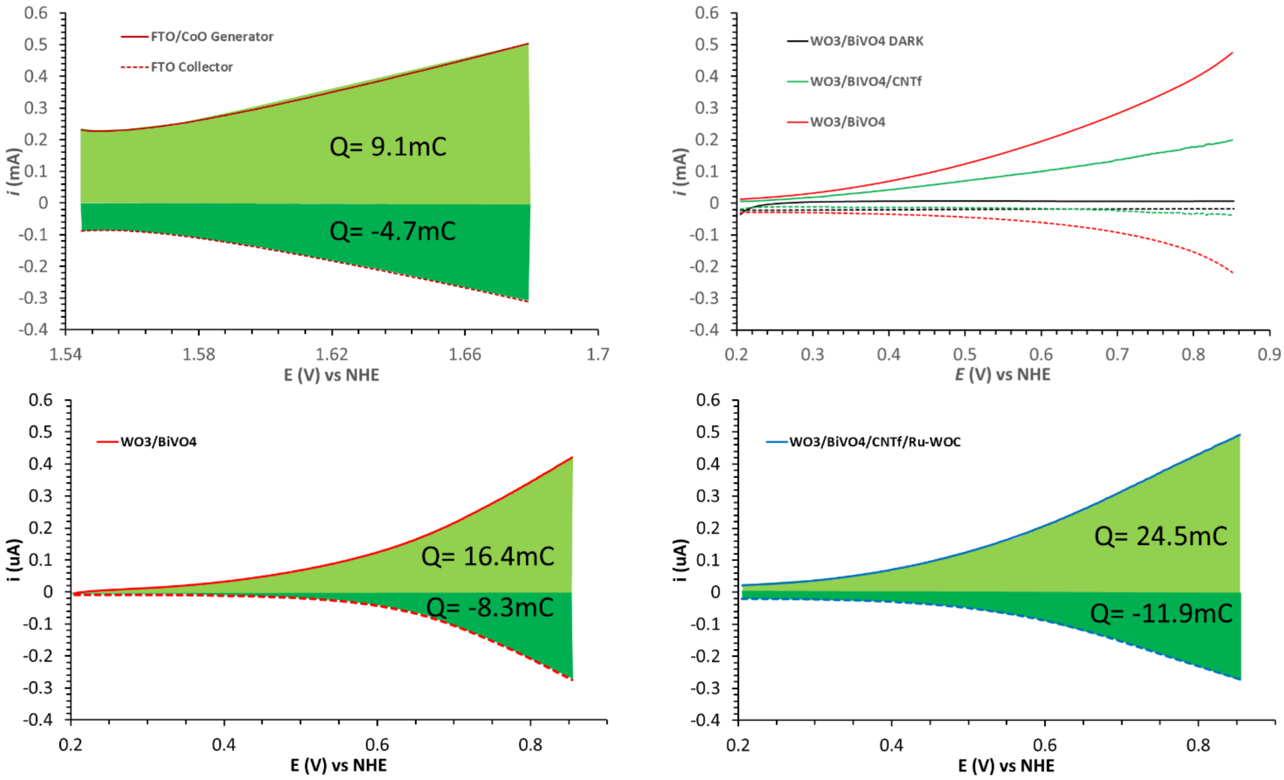

Figure S13. Complementary Generator Collector Experiments. The solid lines correspond to LSV experiments (5 mV/s) in the generator electrode and the dashed lines correspond to simultaneous bulk electrolysis experiments in the collector electrode (applied potential = -0.355 vs NHE). **Top, left)** Calibration of the Generator-Collector Method with a FTO/Cobalt oxide[9] generator electrode to calculate the Efficiency of Oxygen Reduction of the experimental set-up. See also page S13. **Top, right)** Analysis of $WO_3/BiVO_4/CNT_f$ vs $WO_3/BiVO_4$ by the Generator-Collector Method. This experiment proves that the $WO_3/BiVO_4/CNT_f$ does not generate any species detectable in the collector electrode (green dashed line). Thus, the photocurrent observed in the linear sweep voltammetry of the electrode $WO_3/BiVO_4/CNT_f$ (green solid line) must be due to a non-faradaic process or to the formation of oxidized species that are not detectable in the collector electrode. Indeed, in the absence of the Ru-WOC it is possible that the oxidizing holes generated in the photoactive layer ($WO_3/BiVO_4$) may oxidize the carbon nanotubes.[1,11] **Bottom)** Integrated currents of the G-C experiments in Figure 4 of main manuscript for $WO_3/BiVO_4$ **(left)** and $WO_3/BiVO_4/CNT_f$/Ru-WOC **(right)**. See also page S13.

Calculation of faradaic efficiency using Generator-Collector Method:

The faradaic efficiency values were obtained using the following formula:

$$\eta_{O_2} = \frac{-Q_{CPE}}{Q_{LSV}} \cdot \frac{1}{\eta_{coll}}$$

Where Q_{LSV} is the integrated photocurrent measured in the generator electrode, Q_{CPE} is the integrated current measured in the collector electrode and η_{coll} is Efficiency of Oxygen Reduction measured in our experimental set-up. Q_{LSV}, Q_{CPE} and η_{coll} were calculated using the following formulas:

$$Q_{LSV} = \int_{E_0}^{E} \frac{i_{ox}}{v_{scan}} dE$$

$$Q_{CPE} = \int_{t_0}^{t} i_{red} \cdot dt$$

$$\eta_{coll} = \frac{-Q_{FTO}}{Q_{FTO/CoOx}}$$

Where i_{ox} is the intensity measured in the generator, v_{scan} is scan-rate, i_{red} is the current measured in the collector, Q_{FTO} is the integrated current measured in the collector and $Q_{FTO/CoOx}$.

Experimental Data from Figure S13:

- Efficiency of Oxygen reduction:

$$\eta_{coll} = \frac{-(-4.7mC)}{9.1mC} = 0.52$$

- Faradaic Efficiency of $WO_3/BiVO_4$:

$$\eta_{O_2} = \frac{-(-8.33mC)}{16.42mC} \cdot \frac{1}{0.52} = 0.97$$

- Faradaic Efficiency of $WO_3/BiVO_4/CNT_f$/Ru-WOC:

$$\eta_{O_2} = \frac{-(-11.91mC)}{24.48mC} \cdot \frac{1}{0.52} = 0.94$$

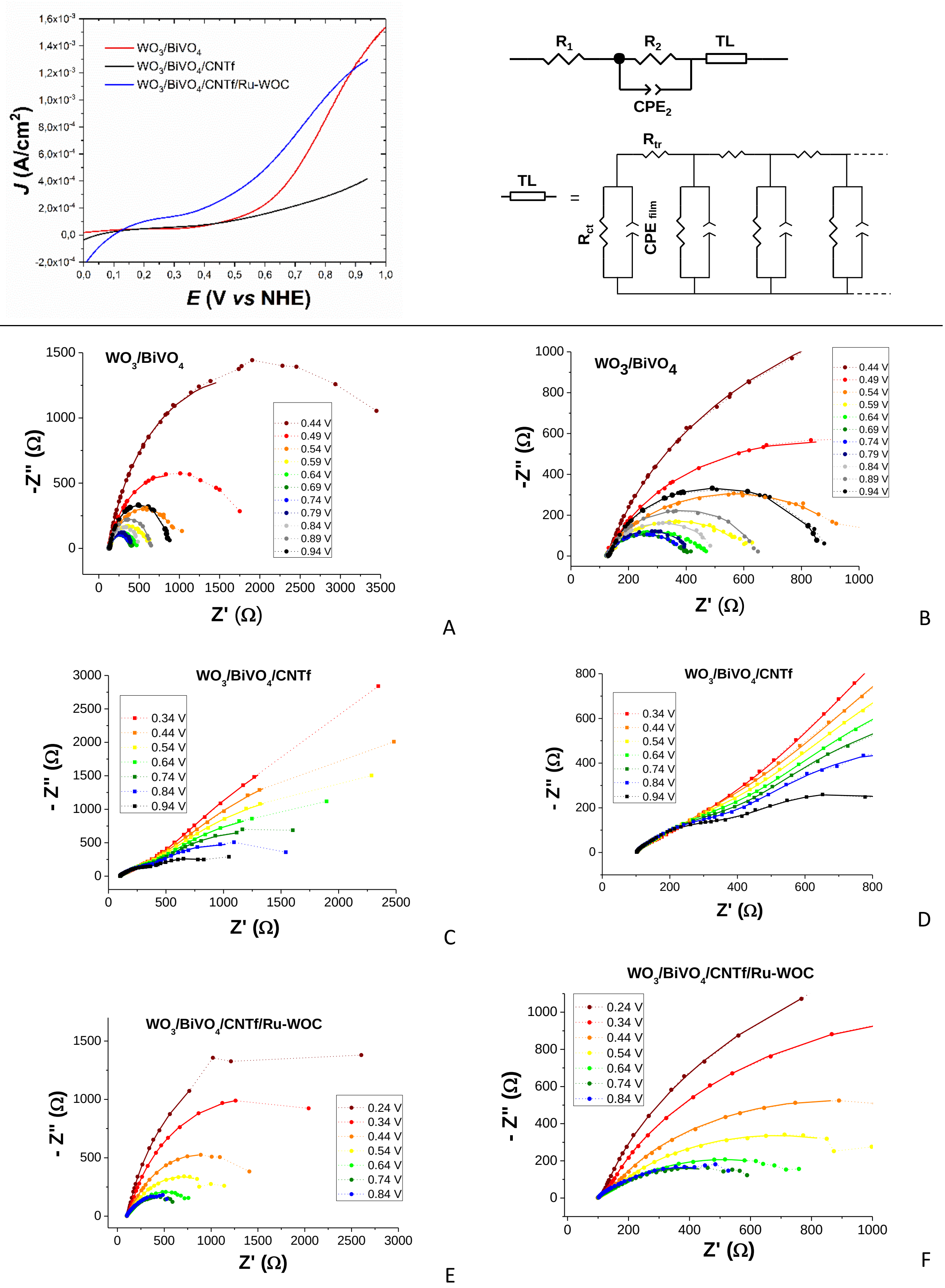

Figure S14. Top) left, J-V curves of the different photoanodes recorded at pH 7 under 1 sun illumination (0.1 W/cm^2 AM1.5G). $WO_3/BiVO_4$ (red), $WO_3/BiVO_4/CNT_f$ (black) and $WO_3/BiVO_4/CNT_f$/Ru-WOC (blue). **Right,** Equivalent circuit used to fit the EIS data of the photoanodes. **Bottom)** Complex plane Nyquist plots for $WO_3/BiVO_4$ (A, zoomed in B), $WO_3/BiVO_4/CNT_f$ (C, zoomed in D) and $WO_3/BiVO_4/CNT_f$/Ru-WOC (E, zoomed in F) photoanodes recorded phosphate buffer (pH 7) under 1 sun illumination and different applied biases (all values *vs* NHE). The corresponding fits are also reported as thick solid lines.

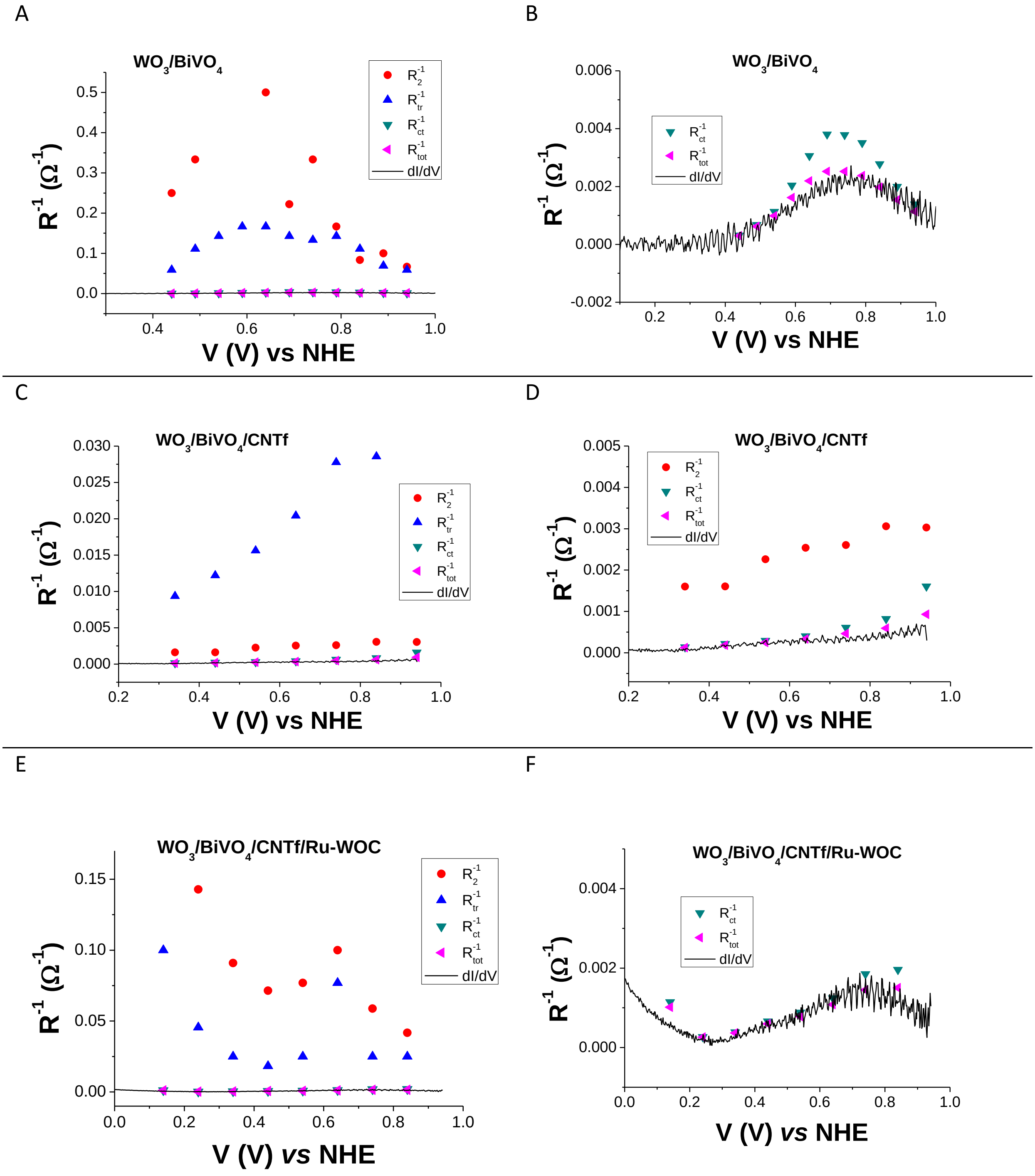

Figure S15. Applied bias dependence of R_{tot}^{-1} (pink triangles), R_2^{-1} (red circles), R_{tr}^{-1} (blue triangles) and R_{ct}^{-1} (green reverted triangles) for $WO_3/BiVO_4$ (A, zoomed in B), $WO_3/BiVO_4/CNT_f$ (C, zoomed in D) and $WO_3/BiVO_4/CNT_f$/Ru-WOC (E, zoomed in F) photoanodes recorded at pH 7 under 1 sun. The resistance values are obtained from the fitting of the EIS data with the equivalent circuit reported in Figure S12 (top). The corresponding derivatives of the J-V curves in Figure S13 (di/dV) are reported as gray solid lines.

Table S1. Resistance values obtained for all the reported photoanodes after the EIS data fit with the equivalent circuit reported in Figure S13.

Electrode	**E (V) *vs* NHE**	**R_1 (Ω)**	**R_2 (Ω)**	**R_{tr} (Ω)**	**R_{ct} (Ω)**	**R_{tot} (Ω)**
$WO_3/BiVO_4$	0.44	121	4	17	3200	3342
"	0.49	121	3	9	1472	1605
"	0.54	121	1	7	884	1013
"	0.59	121	1.5	6	490	618.5
"	0.64	121	2	6	327	456
"	0.69	122	4.5	7	263	396.5
"	0.74	122	3	7.5	264	396.5
"	0.79	123	6	7	285	421
"	0.84	124	12	9	360	505
"	0.89	125	10	14.5	500	649.5
"	0.94	126	15	17	721	879
$WO_3/BiVO_4$/CNTf	0.34	96	625	107	7273	8101
"	0.44	97	623	82	4625	5427
"	0.54	97	442	64	3408	4011
"	0.64	97	394	49	2469	3009
"	0.74	99	384	36	1636	2155
"	0.84	98	327	35	1219	1679
"	0.94	99	330	24	622	1075
$WO_3/BiVO_4$/CNTf/Ru-WOC	0.14	98	5	10	873	986
"	0.24	98	7	22	3729	3856
"	0.34	97	11	40	2590	2738
"	0.44	96	14	55	1510	1675
"	0.54	96	13	40	1133	1282
"	0.64	97	10	13	804	924
"	0.74	92	17	40	540	689
"	0.84	92	24	40	510	666

Table S2. Capacitance values obtained for all the reported photoanodes after the EIS data fit with the equivalent circuit reported in Figure S13.

Electrode	**E (V)** ***vs*** **NHE**	**CPE$_2$ (F)**	**CPE$_{film}$ (F)**
$WO_3/BiVO_4$	0.44	9.9E-5	1.95E-4
“	0.49	1E-4	2.11E-4
“	0.54	3.78E-5	2.61E-4
“	0.59	4.49E-5	2.34E-4
“	0.64	2.72E-5	1.84E-4
“	0.69	1.47E-5	1.34E-4
“	0.74	3.19E-5	1.16E-4
“	0.79	3.37E-5	9.16E-5
“	0.84	3.01E-5	7.57E-5
“	0.89	9.23E-4	6.84E-5
“	0.94	1.32E-5	5.75E-5
$WO_3/BiVO_4$/CNTf	0.34	5.55E-4	6.23E-4
“	0.44	4.66E-4	6.64E-4
“	0.54	3.46E-4	6.44E-4
“	0.64	2.82E-4	6.9E-4
“	0.74	2.39E-4	7.33E-4
“	0.84	1.99E-4	7.86E-4
“	0.94	1.99E-4	1.15E-3
$WO_3/BiVO_4$/CNTf/Ru-WOC	0.14	2.73E-4	5.37E-4
“	0.24	3.67E-4	4.71E-4
“	0.34	4.08E-4	4.73E-4
“	0.44	2.87E-4	4.85E-4
“	0.54	8.68E-5	4.59E-4
“	0.64	4.4E-5	4.03E-4
“	0.74	4.45E-5	2E-4
“	0.84	3.2E-5	1.11E-4

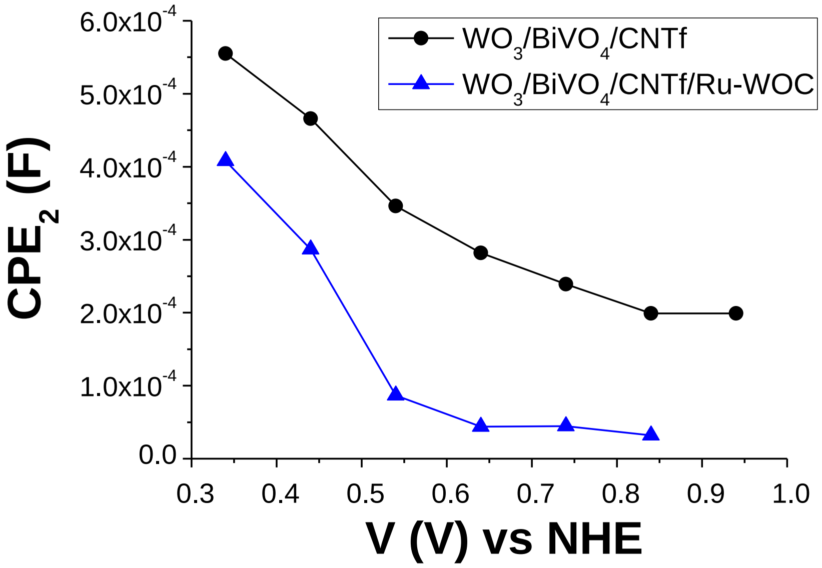

Figure S16. Dependency of the CPE_2 capacitance on the applied potential for $WO_3/BiVO_4/CNT_f$ (black) and $WO_3/BiVO_4/CNT_f$/Ru-WOC (blue).

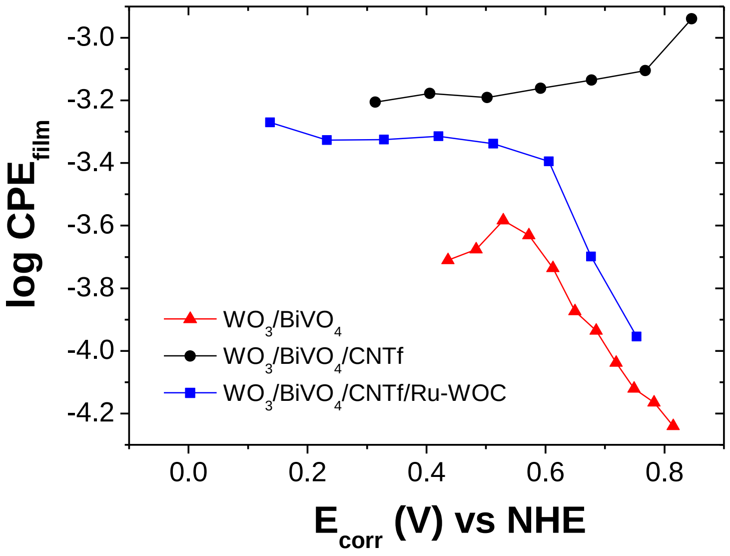

Figure S17. Dependency of the logarithm of the CPE_{film} capacitance on the applied potential corrected for the iR drop.

References

(1) Creus, J.; Matheu, R.; Peñafiel, I.; Moonshiram, D.; Blondeau, P.; Benet-Buchholz, J.; García-Antón, J.; Sala, X.; Godard, C.; Llobet, A. *Angew. Chem. Int. Ed.* **2016**, *55*, 15382.

(2) Cristino, V.; Marinello, S.; Molinari, A.; Caramori, S.; Carli, S.; Boaretto, R.; Argazzi, R.; Meda, L.; Bignozzi, C. A. *J. Mater. Chem. A* **2016**, *4*, 2995.

(3) Seabold, J. A.; Choi, K.-S. *J. Am. Chem. Soc.* **2012**, *134*, 2186.

(4) Chen, Z. D., H. N.; Miller, E.; Springer: 2013.

(5) Hong, S. J.; Lee, S.; Jang, J. S.; Lee, J. S. *Energy Environ. Sci.* **2011**, *4*, 1781.

(6) Reguero, V.; Alemán, B.; Mas, B.; Vilatela, J. J. *Chem. Mater.* **2014**, *26*, 3550.

(7) Sherman, B. D.; Sheridan, M. V.; Dares, C. J.; Meyer, T. J. *Anal. Chem.* **2016**, *88*, 7076.

(8) Kirner, J. T.; Finke, R. G. *ACS Appl. Mater. Interfaces* **2017**, *9*, 27625.

(9) Kanan, M. W.; Nocera, D. G. *Science* **2008**, *321*, 1072.

(10) Matheu, R.; Ertem, M. Z.; Benet-Buchholz, J.; Coronado, E.; Batista, V. S.; Sala, X.; Llobet, A. *J. Am. Chem. Soc.* **2015**, *137*, 10786.

(11) Matheu, R.; Moreno-Hernandez, I. A.; Sala, X.; Gray, H. B.; Brunschwig, B. S.; Llobet, A.; Lewis, N. S. *J. Am. Chem. Soc.* **2017**, *139*, 11345.

(12) Francàs, L.; Matheu, R.; Pastor, E.; Reynal, A.; Berardi, S.; Sala, X.; Llobet, A.; Durrant, J. R. *ACS Catal.* **2017**, *7*, 5142.